# AIAA 93-4861

# Induced Surface Pressure Distribution of a Subsonic Jet in a Crossflow

Robert F. Dennis, Jin Tso;
California Polytechnic State
Univ., San Luis Obispo, CA and
Richard J. Margason;
NASA Ames Research Center,
Moffett Field, CA

# 1993 International Powered Lift Conference
## December 1-3, 1993 / Santa Clara, CA

# INDUCED SURFACE PRESSURE DISTRIBUTION
# OF A SUBSONIC JET IN A CROSS FLOW

Robert F. Dennis[*] and Jin Tso[**], Calif. Polytechnic State University, San Luis Obispo, CA

Richard J. Margason[‡], NASA Ames Research Center, Moffett Field, CA

## ABSTRACT

An experimental investigation of the flow interaction of a 5.08 cm (2.00 in.) diameter round subsonic cold jet exhausting perpendicularly to a flat plate in a subsonic crossflow was conducted in the NASA Ames 7x10 Ft. Wind Tunnel No. 1. Plate surface pressures were measured at 400 locations in a 30.48 cm (12.0 in.) concentric circular array about the jet exit. The measurements are discussed for jet-to-crossflow velocity ratios from 4 to 12. The pressure measurements are compared with previous experiments and numerical solutions. Schleiren photographs of the jet plume shape were obtained. The surface pressure results compare closely with previous work and provide a useful characterization of jet induced surface pressures. The measurements demonstrate the primary influence of jet velocity ratio in determining such surface pressures.

## NOMENCLATURE

$C_p$    Induced coefficient of pressure due to jet flow

D    Jet diameter at exit

$M_j$    Jet Mach number at exit

R    Effective velocity ratio, $(V_j/V_\infty) * \sqrt{(\rho_j/\rho_\infty)}$

$Re_D$    Reynolds number based on D and $V_\infty$

r    Radial location of pressure port from jet centerline

V    Velocity

$\theta$    Angular location, clockwise from leading edge

$\rho$    Density

$\infty$    Subscript indicating freestream condition

j    Subscript indicating jet exit condition

## INTRODUCTION

The goal of this study was to provide additional improved data describing the surface pressure patterns created by a round subsonic cold jet exhausting perpendicularly from a flat plate in a subsonic crossflow. The jet-in-cross-flow (JICF) model provides a geometrically simple case relevant to powered lift applications such as transitional flight of a V/STOL aircraft out of ground effect. JICF phenomena also have applications in other areas, including reaction control, fluid dispersion, and

* Graduate Assistant, Student Member AIAA
** Associate Professor, Senior Member AIAA
‡ Aeronautical Engineer, Associate Fellow AIAA

combustion. General information on JIFC research may be obtained from a comprehesive survey by Margason[1]. Previous work has been done on JICF surface pressure distribution by R. Fearn, et.al.[2] and by K. Aoyagi, et. al.[3] The motivation for the present study was to assist in the validation of computational fluid dynamics (CFD) codes with respect to complex flowfields by obtaining data to evaluate the capability of CFD to predict important flow parameters. In conjunction with this study, CFD studies have been done of a comparable JICF configuration by Chiu, et.al.[4] and by Margason and Tso[5].

General Features of a Jet-In-Cross-Flow. Figure 1 shows the general flowfield features created by a circular jet exhausting perpendicularly into a crossflow. The dominant feature is the deflection of the jet downstream into a curved path by the pressure and shearing forces exerted on the jet by the mean flow. The deflection of the jet is accompanied by the distortion of the jet cross-section and the creation of lateral counter-rotating vortices by the shearing action of the mean flow on the jet boundary. The shear layers so formed progressively roll up into a pair of vortices which propagate below and to the sides of the centerline of the curved jet path. The potential core of the jet decays rapidly, and the vortex pair becomes the primary jet plume feature within a few jet diameters.

A secondary feature is a horseshoe vortex at the plate surface created by the deflection and rolling up of the plate boundary layer by the jet. Behind the horseshoe vortex is a complex and unsteady wake region. The flow in this wake region reflects the combined effects of flow entrainment by the jet and the shedding of vortices as the cross flow separates from the jet near the jet trailing edge[6,7].

Correlation Parameter. The effective velocity ratio is the most suitable parameter for correlating the effect of variation in size, density, and velocity in the jet-in-a-crossflow. This is defined as the square root of the ratio of the jet dynamic pressure to the dynamic pressure of the undisturbed freestream:

$$R = \frac{V_j}{V_\infty}\sqrt{\frac{\rho_j}{\rho_\infty}}$$

Work by Williams and Wood[8] has shown that R effectively accounts for the effect of variations in density and temperature between jet and freestream, and is a more suitable parameter than a simple ratio of velocity. In the present investigation, the jet total temperature was approximately equal to the freestream value, and temperature variation was due primarily to isentropic expansion. Transition in jet-borne VSTOL aircraft such as the Harrier occurs at values of R of about 3.5 and more.

Induced Pressures. The pressure distribution induced by a JICF has been studied by a number of investigators[2,9,10]. A comparison of experimental results[1] shows that transducer uncertainties are significant in areas with shallow pressure gradients. Figure 2 shows that the discrepancy between experimental results is greatest in the wake region behind the jet exit. The data of Fearn and Weston[2] show a larger negative pressure region, possibly due to higher Reynolds numbers.

CFD Studies. CFD studies using finite difference representations of the Navier-Stokes equations have been used effectively to characterize a large portion of the JICF velocity and pressure field[1]. A recent study by Chiu, et al[4], used

separate grids to represent the jet plume and the surrounding flowfield, with the solutions being interpolated by the Chimera technique[11], and compares the effects of a variety of different grids, turbulence models, and boundary conditions.

## EXPERIMENTAL SETUP AND TEST PROCEDURE

Wind Tunnel. The present experimental investigation was conducted in the NASA/Ames Research Center subsonic 7x10 foot Wind Tunnel No. 1. The tunnel is an unpressurized closed-return, closed throat type and is of rectangular cross-section. The tunnel is used for general aerodynamic research at velocities up to 200 knots. Futher information on this wind tunnel and its flow characteristics is available in reference 12.

Model Description. The model geometry is depicted in Figure 3. The model consisted of a rectangular groundplane with a jet blowing perpendicularly from the upper surface at the one-third chord position. The ground plane was supported 2.58 ft above the tunnel floor on 4 tubular steel legs of streamline cross section. The groundplane consisted of a 0.083 ft. thick sandwich plate of aluminum face sheets bonded to a plywood core. A 0.167 ft. wide leading edge strip was constructed of fiberglass covered wood and was faired smoothly into the plate. The trailing edge strip was of the same construction as the leading edge and was 0.5 ft. wide. The groundplane tips were formed of semi-circular section wood. The total groundplane chord was 4.5 ft. and the total span was 4 ft.

The jet exit at the groundplane surface was sharp cornered, perpendicular to the surface, and was 0.167 ft. in diameter. The jet exit was at the center of the groundplane span, and was located at the one-third chord location, 1.5 ft. aft of the leading edge of the groundplane. The nozzle and plenum supplying high velocity air flow to the jet were mounted underneath the groundplane and extend beneath the tunnel floor through removable access plates. That portion of the nozzle and plenum above the tunnel floor were contained in an aluminum fairing which was 1.1 ft. thick, and which extended from 0.5 ft. aft of the leading edge to the trailing edge of the groundplane. The groundplane as a unit was aligned with the test section centerline and was parallel to the tunnel floor.

Jet and Air Supply Description The jet exit consisted of an integral 0.167 ft. long straight cylindrical nozzle extension clamped to the discharge end of the nozzle, and was of the same diameter as the nozzle end. The aluminum nozzle was 0.75 ft. long and had a 14.5:1 convergent contraction which faired smoothly into the nozzle extension. The nozzle was supplied by a cylindrical steel plenum chamber 1.83 ft. long and of 0.635 ft. inside diameter. The flow in the plenum was conditioned by a graded series of perforated plates and turbulence screens. The wind tunnel high pressure air supply was from a large 3000 psi storage tank located outside the tunnel, and the air was heated using a electrical heater system. The plenum pressure was regulated by primary and secondary pressure reducing valves as needed to obtain the desired jet exit velocity Downstream from the secondary pressure reducer was an orifice plate flow meter which was used as a quantitative check on jet dynamic pressure calculations.

Groundplane Instrumentation. The surface pressure measurements were made using a radial array of 400 pressure ports. The array was divided along the line of symmetry of the groundplane. The left side was a dense array containing 330 ports along 15 radial lines, and the right side was a sparce array containing 70 ports along 6 radial lines. The radial port spacing was also varied with the closest spacing near the jet exit where larger gradients were expected. The pressure ports were connected by vinyl tubes to a total of 14 electronically scanned transducer modules which were referenced to the test section static pressure. Individual transducers calibrated to 2.5 psi were assigned to 6 ports at a radial position of 0.58 jet diameters, in the 75° to 105° and -60° to -120° angular positions, where the peak suction pressure was expected to exceed the calibration range of the transducers (0.72 psi).

Wind Tunnel Instrumentation. The wind tunnel is equipped with a permanently installed dedicated data acquisition and instrumentation system. The system includes a mini-computer, data interface, calibration units, data acquisition software, and the instrumentation required to determine tunnel test section freestream conditions. The software computes the test section density and dynamic pressure using calibration polynomials developed for this wind tunnel system[12].

Jet Instrumentation. The jet exit conditions were determined by means of a thermocouple and a static pressure port located in the plenum chamber immediately upstream of the jet nozzle contraction. Due to the nozzle contraction ratio of 14.5:1 and the density change across the nozzle, the plenum chamber velocity was only approximately 47 fps at a value of $M_j$ of 0.91, the highest jet exit Mach number used in the investigation. At this plenum velocity, the plenum temperature and static pressure measurements accurately represented the total pressure and stagnation temperature. The isentropic relationships[13] were incorporated into the data acquisition software to compute jet exit velocity, density, dynamic pressure and Mach number. In a previous investigation by Fearn and Weston[14] using a geometrically similar JICF model the jet exit velocity profile was determined by dynamic pressure measurements. It was shown that the actual jet exit velocity is accurately predicted by the assumption of isentropic expansion across the nozzle, and that the velocity profile was quite flat.

The nozzle pressure ratio used to calculate jet exit conditions was the ratio of plenum chamber total pressure to the freestream static pressure measured at the entrance to the test section. The values of the jet exit conditions based on isentropic assumptions were confirmed qualitatively by the mass flow measurements from the high pressure air system. The JICF model used in the present investigation was used in previous investigations[3,6,15]. In these investigations the test section freestream static pressure was used to determine R from isentropic expansion relationships.

Measurement Methodology. .The measurements of groundplane surface pressures was made over a range of jet Mach numbers and effective velocity ratios which was selected to determine the effect of these parameters on surface pressure. The range of effective velocity ratios was selected to represent the changing velocity of a VSTOL aircraft in transition between hover and wing borne flight. The matrix of test conditions included Mach numbers of 0.50, 0.74 and 0.91 and effective velocity ratios of 4, 6, 8, and 12. The combination of the $M_j$ = 0.91 and R = 4 would have resulted in peak pressures exceeding the calibration range of the transducers, and was not tested. The freestream dynamic pressures ranged from 2.71 psf to 54.26 psf, corresponding to a velocity range from 47.7 fps to 217.1 fps. To assure a consistently turbulent groundplane boundary layer, an abrasive grit trip strip was installed near the leading edge.

In addition to the test measurement matrix described above, measurements without jet flow were made. Due to blockage effects of the model supports and nozzle fairing, a small induced upwash at the groundplane leading edge was expected to create a chordwise pressure gradient over the groundplane in the "jet-off" condition. These jet-off measurements were used to distinguish the effect of jet interaction from the effect of model blockage and alignment. The term "induced pressure" is used here to refer to the net change in pressure between the jet-on and jet-off condition. The jet-off measurements included the full range of freestream

2

dynamic pressures used in the jet-on measurements. This allowed the comparison for each data point to be made with a jet-off measurement taken at the same freestream velocity used with the jet on, in order to minimize scale effects due to transducer sensitivity and plate boundary layer thickness.

Data Acquisition. Data was acquired using the permanently installed data acquisition system in conjunction with the PSI 8400 integrated calibration and data acquisition system, which was used to take data from the groundplane pressure transducer modules. The measurements were time averaged over a period of 20 seconds. Due to system limitations, the data for freestream and jet flow conditions as well as the 6 individual groundplane transducers could not be acquired at the same time as the groundplane pressure data. This data was acquired immediately following the groundplane pressure data, and was also time averaged over 20 seconds.

## RESULTS AND DISCUSSION

Schlieren Photography. Figures 4 and 5 show schlieren photographs taken of the jet exit and plume region at selected effective velocity ratios. The schlieren system was designed for the 7x10 ft wind tunnel, and has a circular field of view of about 17 inches. The image is recorded by a polaroid film pack camera using ASA 1000 film. All photographs in the were made at a jet Mach number of 0.94. This was the highest Mach number used in surface pressure measurements, and was selected to maximize density gradients in the jet plume, without causing localized shock structures near the jet exit.

Figure 4 shows a schlieren photograph of the jet plume at R = 4.65, with $M_j$ = 0.95. The leading edge of the jet can be seen to develop roll-like structures similar to the ring vortices present in the turbulent mixing of free jets. These structures decay rapidly. The plume can be seen to become very broad within a few jet diameters as the vortex pair propagates downstream below the jet centerline. Figure 5 shows a schlieren photograph of the jet plume at R = 6.49, with $M_j$ = 0.94. The plume path curvature can be seen to be less than in Figure 4. The development of the lateral shear layers can be seen more clearly than at R = 4.65. Distinct wave-like structures can be seen separating from jet plume in the wake region.

Pressure Distribution Pattern. Figure 6 is a series of plots of jet induced pressure coefficient plotted along radial rays for angles from 0 to 180 degrees at R = 6 and $M_j$ = 0.94. The radial location of the jet lip is shown as a vertical dashed line in each plot. The general trends seen at R = 6 are representative of the trends at the other effective velocity ratios tested.

Along the 0° azimuth, figure 6 shows that the $C_p$ value does not approach unity at the jet leading edge and the maximum value of $C_p$ is about 0.5. Due to jet entrainment of flow by the jet shear layer, the velocity does not approach zero as would be the case at a stagnation point on a solid body, As expected, the $C_p$ value approaches zero as the radial port location increases. At the side of the jet there is a region of intense suction due to the combined effect of deflection of the freestream by the jet and entrainment of flow by the jet shear layer. Along the 90° azimuth, figure 6 shows that the values of $C_p$ to be less than -4 near the jet exit, and shows that the pressure gradient is very large in this region. As the azimuth angle increases to 180°, Figure 6 shows that near the trailing edge of the jet the suction becomes less intense, but remains substantial. The radial plots show an inflected portion of the pressure gradient at radial locations distances of less than one jet diameter, for azimuth angles greater than 150 degrees.

Symmetry Plane Comparison. In order to assure that the flow about the model was symmetrical, the sparse field data from the left side was compared with denser data from the comparable

angular position on the right side. Figure 7 shows this comparison for R = 6, for angles of ±10°, ±60°, ±120°, and ±170°. The comparison is quite close throughout this range of azimuth angles, and there are no regions of significant or consistent discrepancy. This implies that the flowfield about the model is symmetrical, at least on a time-averaged basis.

Surface Pressure Contours. Figure 8 through 10 are contour plots of the induced pressure coefficient over a half-plane at R = 6, R = 4 and R = 8. In each of these plots, the freestream direction is indicated by an arrow. The locations of the pressure ports are indicated as dots, and the jet exit lip is outlined as a solid line. The dashed lines in each plot represent comparable experimental data from Fearn and Weston[2]. Some of the deviations of these reference curves are due to round-off precision in the tabular data used for comparison.

Figure 8, showing the contours at R = 6, demonstrates the typical JICF surface pressure distribution. The plot shows a relatively small region at the leading edge of the jet, in which positive pressures prevail. The contour of $C_p$ = 0 is a closed curve, showing that the effect of jet-induced suction predominates over the blockage effect of the jet at distances exceeding two jet diameters in front of the leading edge. The contour of $C_p$ = 0 intersects the jet lip at an azimuth angle of about 25°. The contours in the steep-gradient suction region lateral to the jet are aligned with the maximum extent at approximately the 110° azimuth. As the 180° azimuth is approached, the contours fair to a flat shape in the wake region. In the region of the jet trailing edge near the jet lip the innermost contours can be seen to intersect the jet lip at angles beyond 150°. This corresponds to the inflected portion of the radial distribution plots in Figure 6 discussed above.

Effect of Velocity Ratio. Figures 9 and 10 demonstrate that although the surface pressure distribution at R = 4 and R = 8 is similar to the distribution at R = 6, there are some distinct trends with variation in effective velocity ratio. Figure 11 summarizes these trends and shows two selected $C_p$ contours at effective velocity ratios from 4 to 12. The contours of $C_p$ = 0 shows that the region of positive pressure dramatically contracts as effective velocity ratio increases. The largest change is between values of R of 4 and 6. As the value of R exceeds 4, the region of positive pressure becomes bounded by a closed curve near the leading edge, with negative pressures propagating ahead of the jet at distances of greater than 1.5 D. The contours of $C_p$ = -0.5 shows the overall shape of the suction region. As R increases, the area within the contour moves forward. The greatest change is again between values of R of 4 to 6, with the extended "tail" of the suction region at the trailing edge disappearing as R exceeds 4.

Figure 12 displays the values of $C_p$ at r/D = 0.58, innermost pressure port location, for three representative angular locations, as a function of effective velocity ratio. The curves represent the jet leading edge (0°), the jet trailing edge (180°), and the minimum $C_p$ port (generally 90°, 75° for R = 12). These curves are indicative of the limiting values of $C_p$ as the jet lip is approached. At the jet leading edge, figure 12 shows a gentle trend to lower $C_p$ maxima as R increases, as might be expected due to stronger shearing effects at the jet boundary. At the jet trailing edge, there is a consistent trend to higher $C_p$ values as R increases. The measurements in this location correspond to the data shown in the inflected portion of the radial plots of Figure 6.

In contrast to the consistant trends at the leading and trailing edge, figure 12 shows that the minimum Cp value at the lateral jet lip reaches a well-defined exteme at R = 6. It appears that this ratio of jet-to-freestream velocities may maximize the lateral vortex intensity near the groundplane surface. For values of R > 6 the jet may behave more like a solid body near the

3

groundplane surface, with the development of a dominating plume vortex being delayed to larger vertical distances.

If R continues to increase above 12, the flowfield will gradually approach that of a jet exiting from a plate without crossflow (analogous to hovering flight out of ground effect), although $C_p$ is undefined at this point since it is based on freestream dynamic pressure. In this configuration, a symmetrical finite negative surface pressure pattern would be induced by the jet alone[16]. Figure 12 suggests that the minimum $C_p$ curve initially approaches a limiting value below -3, suggesting that the jet acts to accelerate the freestream in a manner similar to a solid cylinder near the groundplane surface as R exceeds 12. At high values of R the development of the plume vortex may be delayed to larger vertical distances.

Comparison with Other Work. Figures 8 to 10 contain dashed contour lines which represent comparable experimental data from Fearn and Weston[2], obtained at values of R of 4, 6, and 8. This reference data is from a geometrically similar model with D = 4 inches. Some of the deviations of these reference curves are due to the round-off precision in the tabular data used for comparison. In general, the experimental data is in good agreement with the reference data. There are no apparent differences in the contours of a magnitude greater than the uncertainty of the data.

Figure 13 shows a comparison with CFD solutions obtained from related work done a NASA/Ames by Chiu, et al.[4] with the experimental measurements in the present investigation. The plots compare the radial $C_p$ distribution for the 0°, 90°, and 180° azimuths. The experimental measurements are at R = 6 and $M_j$ = 0.74. The CFD solutions were done with the OVERFLOW code at values of R = 6 and $M_j$ = 0.78, with extrapolated outflow boundary conditions. The computational upper and lateral boundaries were z/D = 20 and y/D = 10.

The first CFD solution corresponds to the intermediate density grid 3 solution shown in Figure 14 of Reference 4, using the Baldwin-Lomax turbulence model. The second CFD solution corresponds to the Baldwin-Barth solution shown in Figure 15 of Reference 4, and was computed using the finer pitch grid 2. That studyfound that the solutions of groundplane surface pressure were sensitive to the grid geometry in the shear region, the type of boundary conditions, the turbulence model, and the version of the code used. No single combination of these parameters was found to be superior to all others in comparison with experiment in all regions of the surface pressure signature.

At the 0° azimuth, Figure 13 shows both CFD solutions to be generally close to the experimental values, although the Baldwin-Barth solution is not quite asymptotic to zero as radius becomes large. The value of $C_p$ as the jet exit lip is approached is also higher for the CFD solutions than the experimental value. At the 90° azimuth, again both CFD solutions are generally quite close to the experimental values, and the comparison remains close as the jet lip is approached. At the 180° azimuth, both CFD solutions diverge substantially from the experimental values. It is not surprising that the correlation with experiment is less successful in this region of separated wake flow than in the other quadrants. The Baldwin-Barth solution curve has generally the same shape as the curve of experimental values, but shows a consistent positive pressure offset in comparison to experiment.

Comparison with Solid Cylinder Models. Figures 14 and 15 show plots of the angular distribution of pressure of the innermost circular row of pressure ports (r/D = 0.58) for values of R from 4 to 12 against the experimental and inviscid theoretical results for the surface pressure of a two dimensional solid cylinder[17]. The static pressure at the innermost row of pressure ports is intended to represent the limiting value of

surface pressure near the jet exit. This comparison gives qualitative indication of the relative effect of jet entrainment and flow deflection in producing the observed surface pressure signature, but it should be noted that the analogy of the three dimensional jet to a two dimensional solid cylinder is only an rough approximation. The JICF interaction of free shear layers and the groundplane boundary layer is qualitatively different from boundary layer flow about a 2-D solid cylindrical body.

Figure 14 shows that the general shape of the inviscid model is best approximated at the highest value of R = 12, although the $C_p$ values are consistently more negative. Figure 15 compares the experimental jet induced pressures for values of R of 4 and 12 with experimental solid cylinder data[17]. The cylinder data is shown at both a subcritical Reynolds number ($Re_D$ = 1.9 x $10^5$) and a supercritical Reynolds number ($Re_D$ = 6.7 x $10^5$). It can be seen that the shape of the plot of the data for R = 12 roughly approximates the shape of the supercritical experimental solid cylinder data. At this relatively large value of R the difference between the curve of JICF data and the curve of supercritical cylinder data is generally approximately constant with respect to angular position. It appears that at the higher value of R the surface pressure distribution near the jet lip can be qualitatively viewed as a superposition of the effect of velocity changes due to flow blockage by the jet shape and acceleration by flow entrainment in the shear layer at the jet boundary. This comparison becomes weaker as R decreases.

## CONCLUSION

The goals of this investigation were to obtain improved data on the surface pressure distribution on the groundplane surrounding the jet exit. The measured surface pressure data constitutes a useful extension of prior data. The relatively high precision of the pressure transducers made this possible. The schlieren photographs taken are an effective means of visualizing the jet plume structure.

## REFERENCES

1. Margason, R. J., "Fifty Years of Jet in Cross Flow Research," 72nd AGARD Fluid Dynamics Panel Meeting, Winchester, U.K., April 1993.

2. Fearn, R. L. and Weston, R. P., "Induced Pressure Distribution of a Jet in a Crossflow," NASA TN D-7916, July, 1975

3. Aoyagi, K. and Snyder, P. K., "Experimental Investigation of a Jet Inclined to a Subsonic Crossflow," AIAA-81-2610, December, 1981

4. Chiu, S., Roth, K. R., Margason, R. J., and Tso, J., "A Numerical Investigation of a Subsonic Jet in a Crossflow," AIAA 93-0870, January, 1993.

5. Margason, R. J., and Tso, J., "Subsonic Jet in a Crossflow Numerical Investigation," AIAA Paper No. 93-4861, Dec. 1993.

6. Snyder, P. and Orloff, K. L., "Three-Dimensional Laser Doppler Anemonmeter Measurements of a Jet in a Crossflow," NASA TM-85997, 1984.

7. Soullier, A., "Testing at S1.MA for Basic Investigations on Jet Interactions;Distributions of Pressures and Velocities in the Jet Using the Ideal Standard Nozzle (in the Unheated State)," NASA TT F-14072, 1972.

8. Williams, J. and Wood, M. N., "Aerodynamic Interference Effects with Jet Lift Schemes on VSTOL Aircraft a Forward Speeds," AGARDograph 103, Aerodynamics of Power Plant Installation, part 2, Oct. 1965, pp 625-651.

9. Bradbury, L. J. S. and Wood, M. N., "The Static Pressure Distribution Around a Circular Jet Exhausting Normally From a Plane Wall Into an Airstream," CP No. 822, British A.R.C., 1965

10. Thompson, A. M., "The Flow Induced by Jets Exhausting Normally From a Plane Wall Into an Airstream," Ph. D. Thesis, Univ. of London, 1971.

11. Benek, J. A., Bruning, P. G. and Steger, J. L., "A 3-D Chimera Grid Embedding Technique," AIAA-85-1523, 1985.

12. Wadcock, A., "The NASA 7-Foot by 10-Foot Wind Tunnel -- Present Flow Quality and Recommendations for Improvement," Analytical Methods Report 8705, July, 1987.

13. Zucrow, M. J. and Hoffman, J. D.,Gas Dynamics, Vol. 1, John Wiley and Sons, New York, 1976

14. Fearn, R. L. and Weston, R. P., "Velocity Field of a Round Jet in a Cross Flow for Various Jet Injection Angles and Velocity Ratios," NASA TP-1506, Oct. 1979.

15. Fearn, R., Doddington, H. and Westphal, R., "LDV Studies of a Jet In a Crossflow," Naval Air Development Center Report No. NADC-80238-60, 1981

16. Gentry, G. L. and Margason, R. J., "Jet Induced Lift Losses on VTOL Configurations Hovering In and Out of Ground Effect," NASA TN-D-3166, Feb. 1966.

17. Schlichting, H., Boundary-Layer Theory, McGraw-Hill Book Co., New York, 1979.
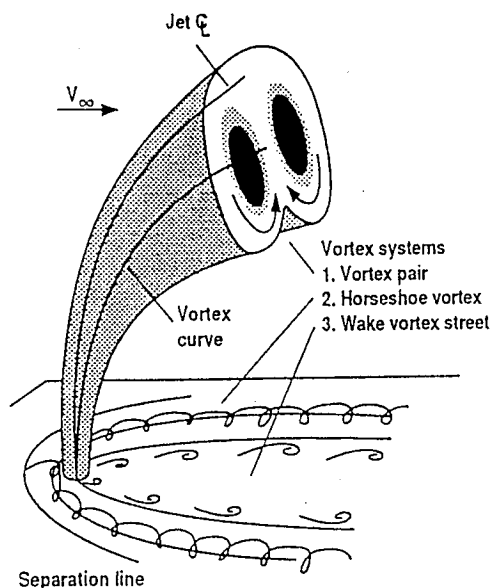
Fig. 1. Components of the flowfield of a jet in a crossflow.
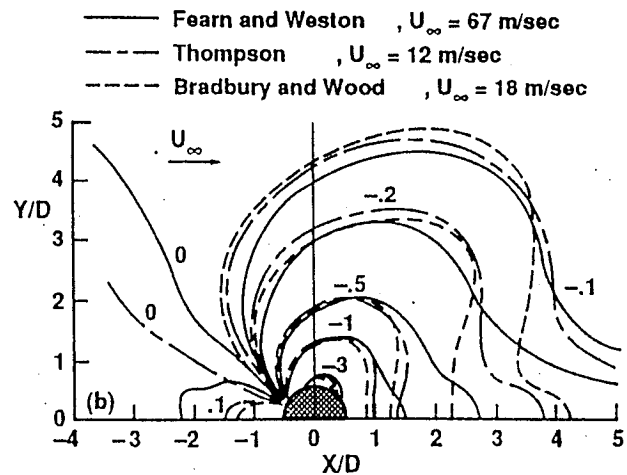


Fig. 2. Comparison of prior experimental surface pressure data[2,9,10].
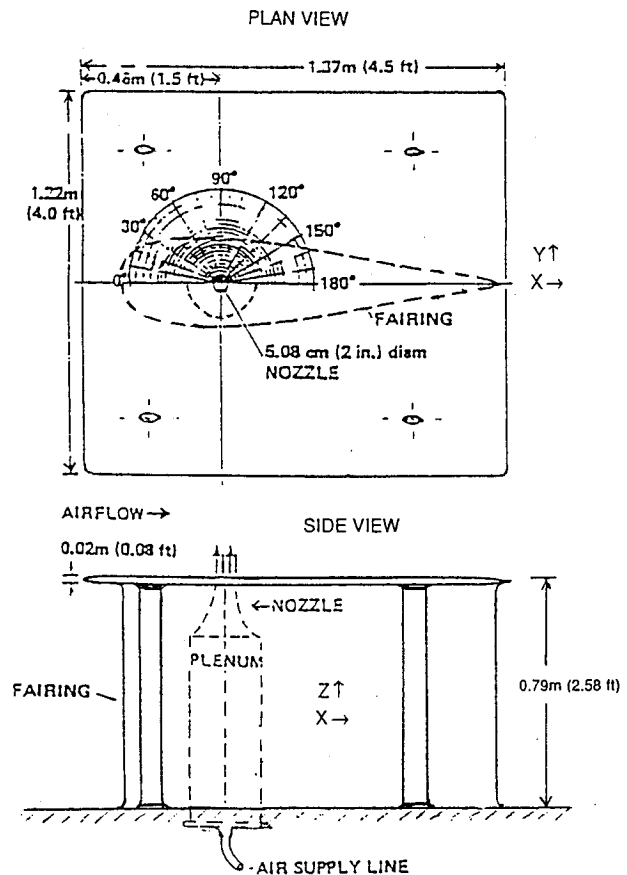


Fig. 3. Diagram of the model.
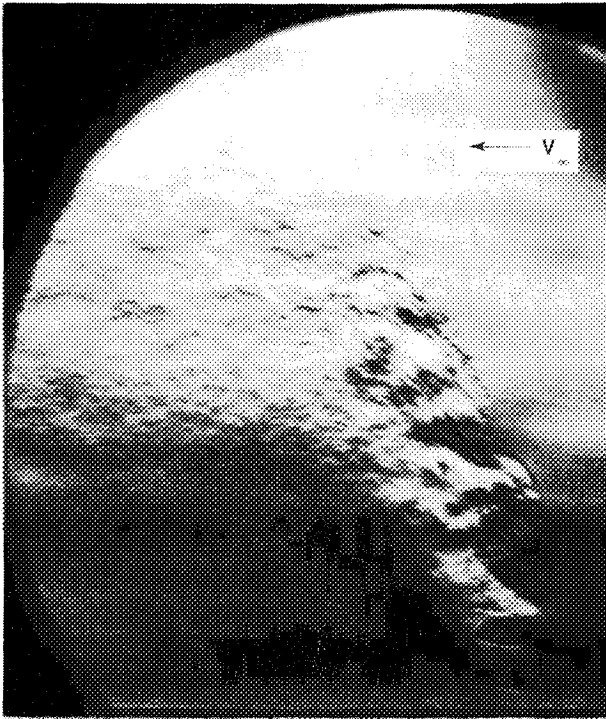
Fig. 4. Schlieren photograph of jet plume at R = 4.65 and $M_j$ = 0.95.
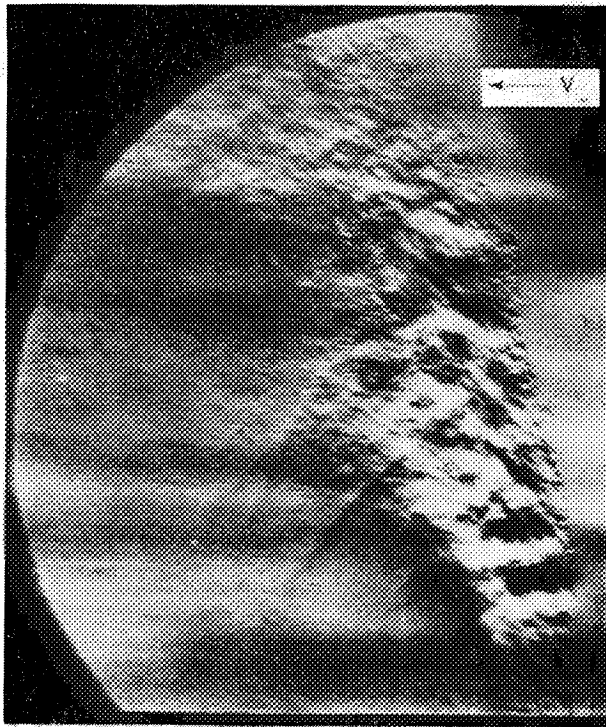


Fig. 5. Schlieren photograph of jet plume at R = 6.49 and $M_j$ = 0.94.
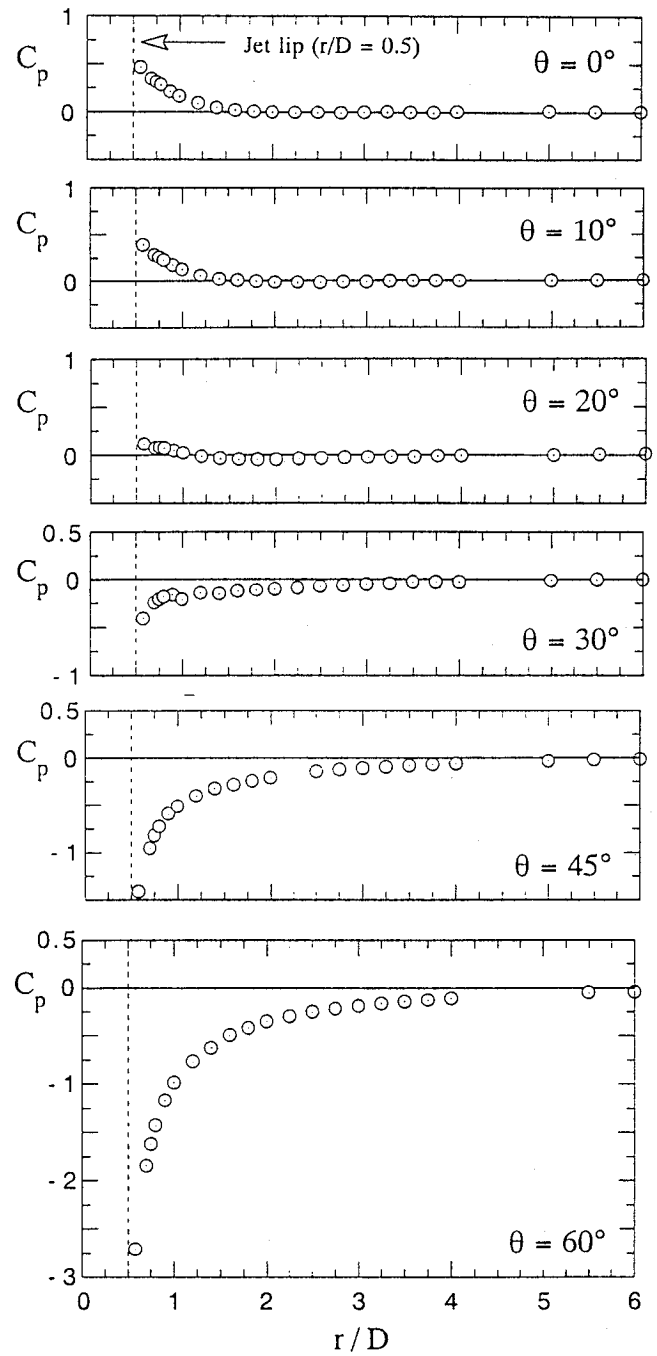


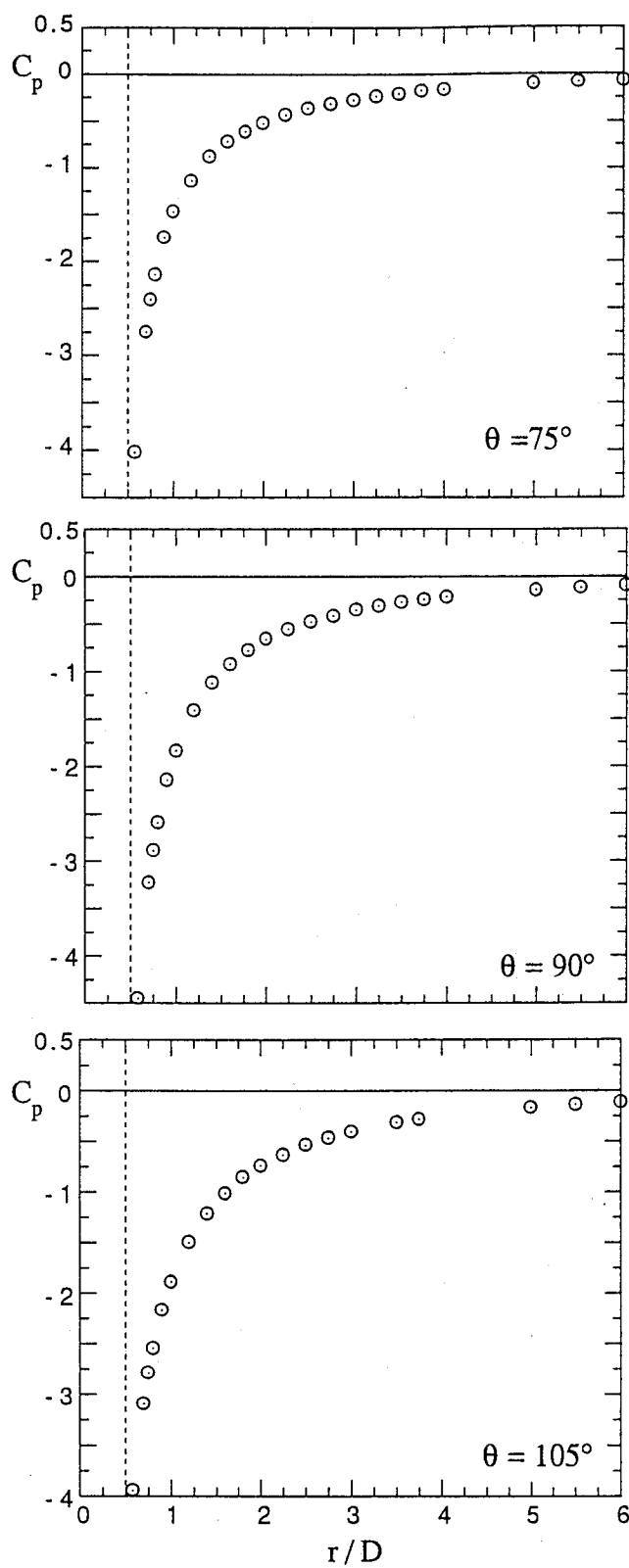Fig. 6. Radial induced pressure distribution by azimuth angle at R = 6.0 and $M_j$ = 0.91.
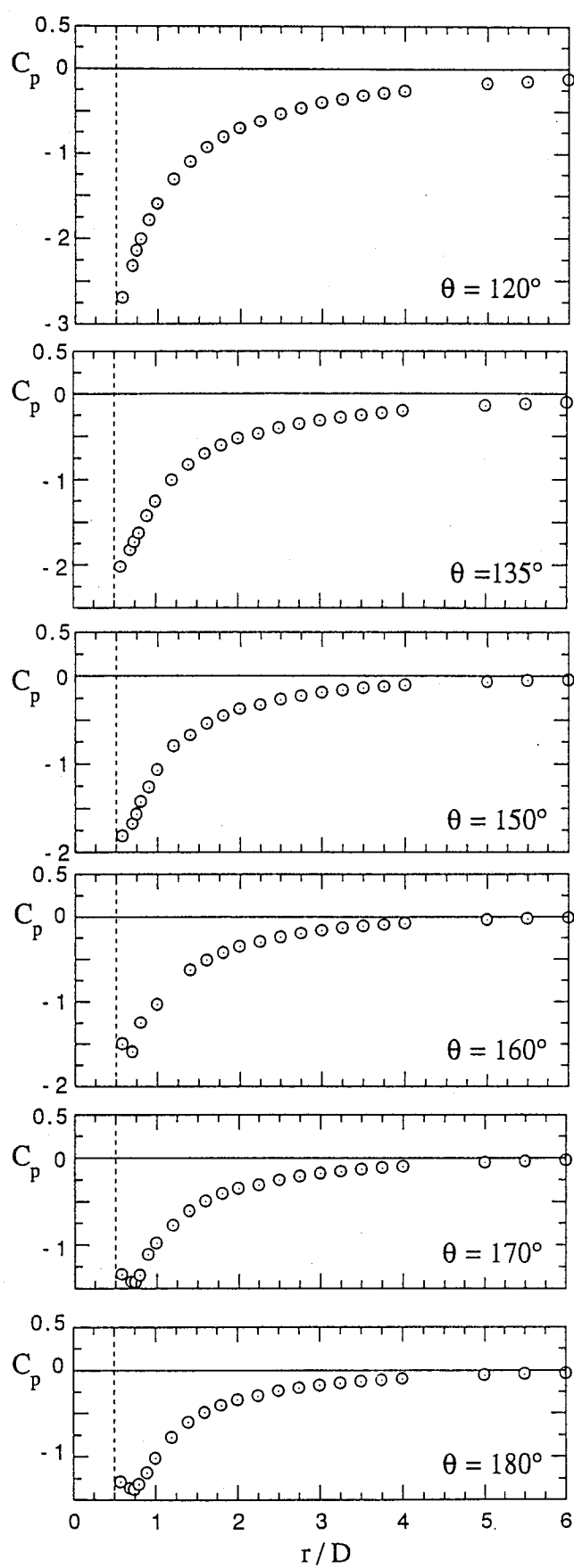
6

Fig. 6 - Continued



Fig. 6 - Continued

7

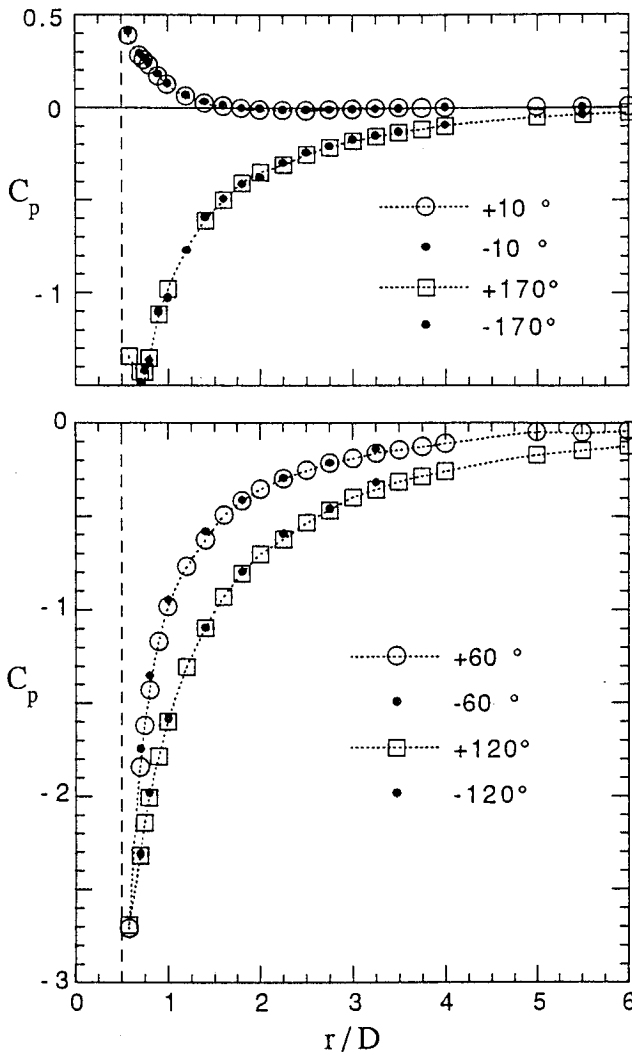Fig. 7. Symmetry comparison of radial $C_p$ distribution at R = 6.02 and $M_j$ = .91 for azimuths from ± 10° to ± 170°.
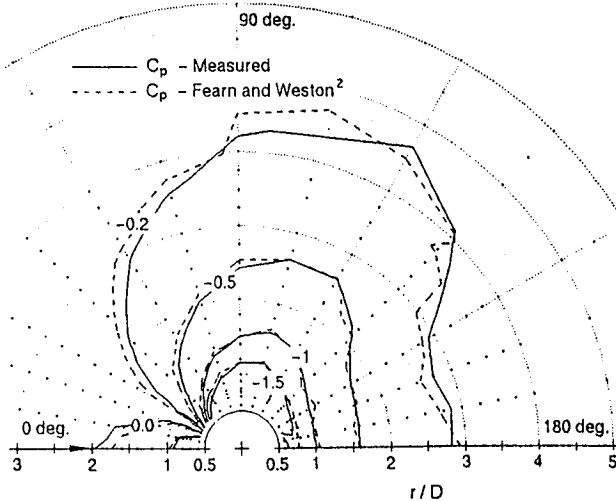


Fig. 8. Comparison of measured Cp with prior experiment[2] at R = 6 and $M_j$ = 0.9.
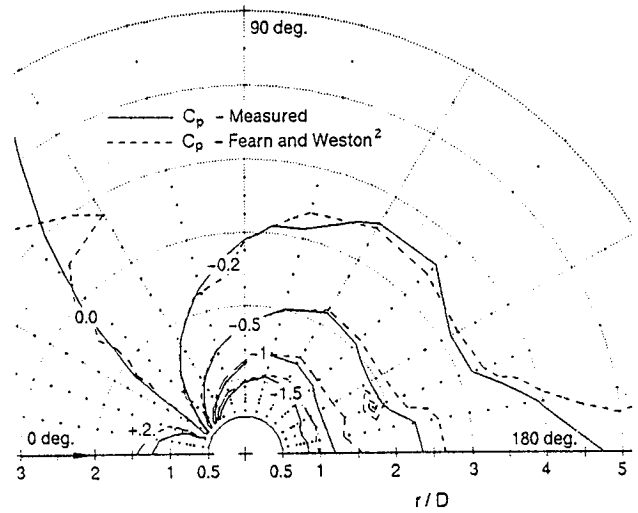


Fig. 9. Comparison of measured Cp with prior experiment[2] at R = 4 and $M_j$ = 0.9.
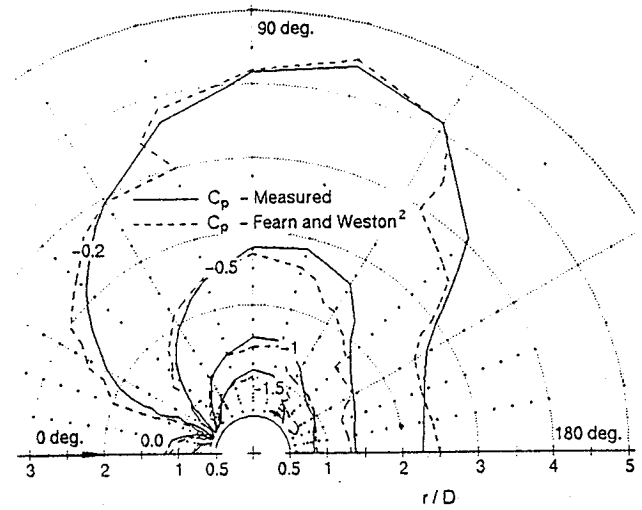


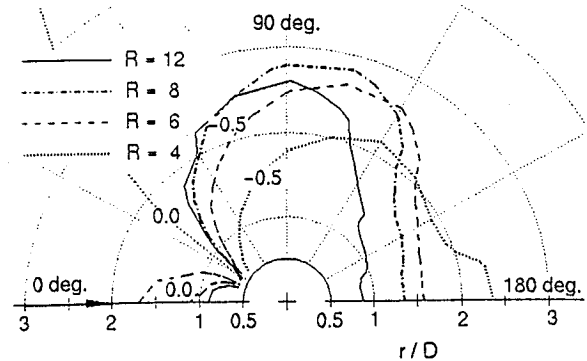Fig. 10. Comparison of measured Cp with prior experiment[2] at R = 8 and $M_j$ = 0.9.



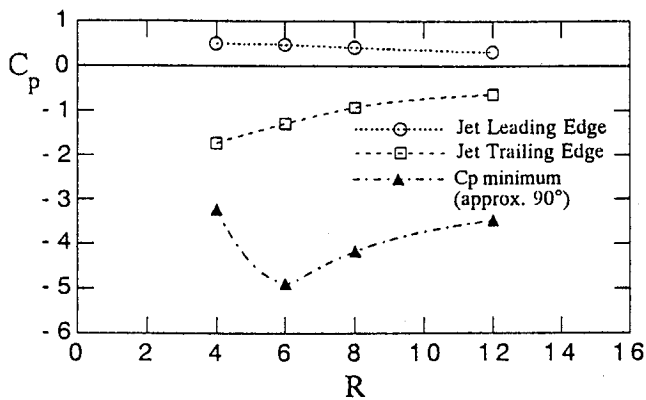Fig. 11. Effect of variation of R for two selected contours of $C_p$ at $M_j$ = 0.74.

8

Fig. 12. $C_p$ near jet exit (r/D = 0.58) at $M_j$ = 0.74 as a Function of Velocity Ratio



(a) 0° azimuth

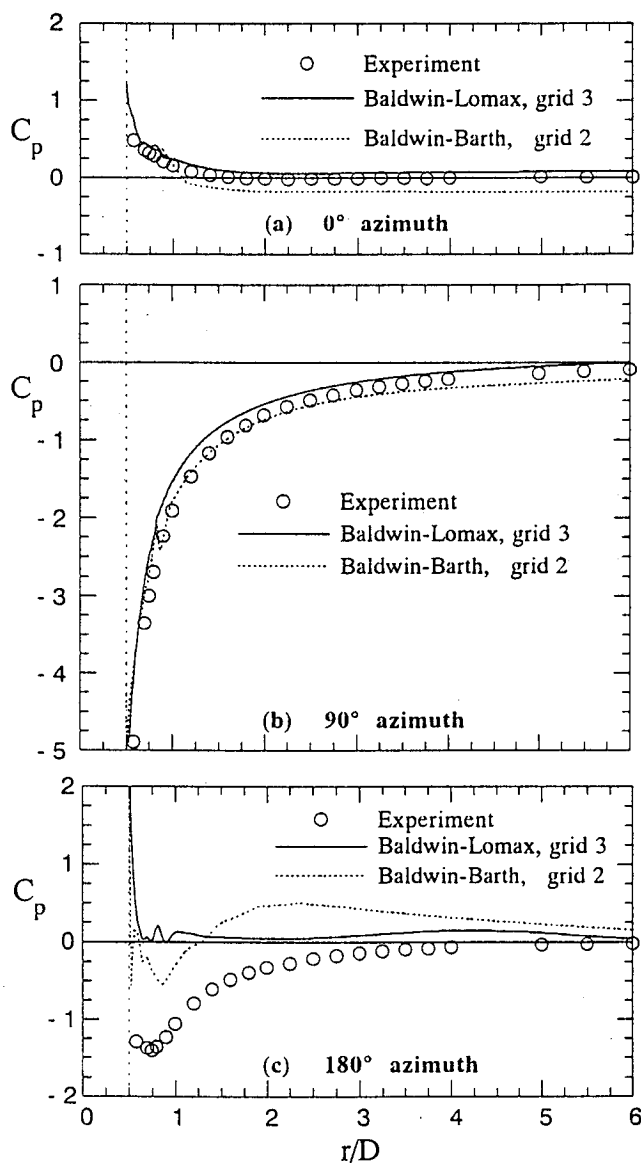(b) 90° azimuth

(c) 180° azimuth

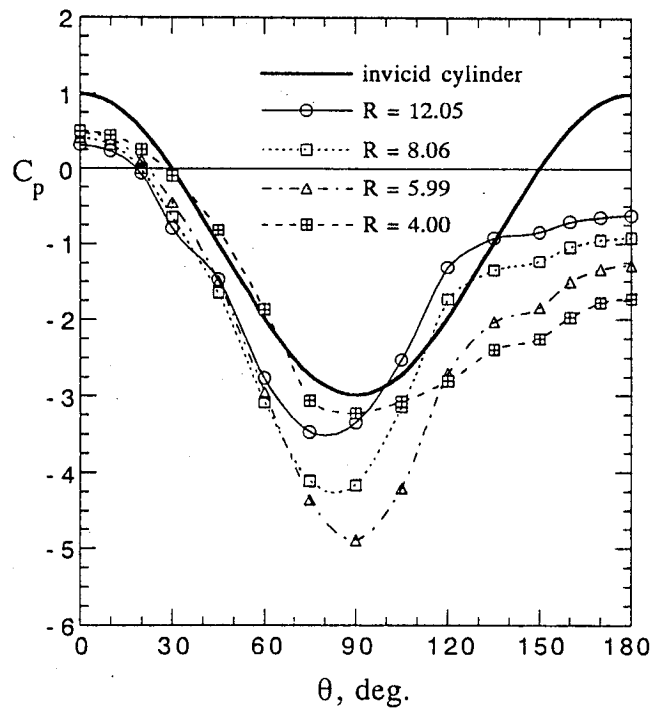Fig. 13. Comparison of measured radial $C_p$ distribution with CFD solutions[4] at R = 6.0, $M_j$ = 0.74.



Fig. 14. $C_p$ near jet exit (r/D = 0.58) at $M_j$ = 0.74 for various velocity ratios compared with 2-D cylinder theorical invicid flow $C_p$.
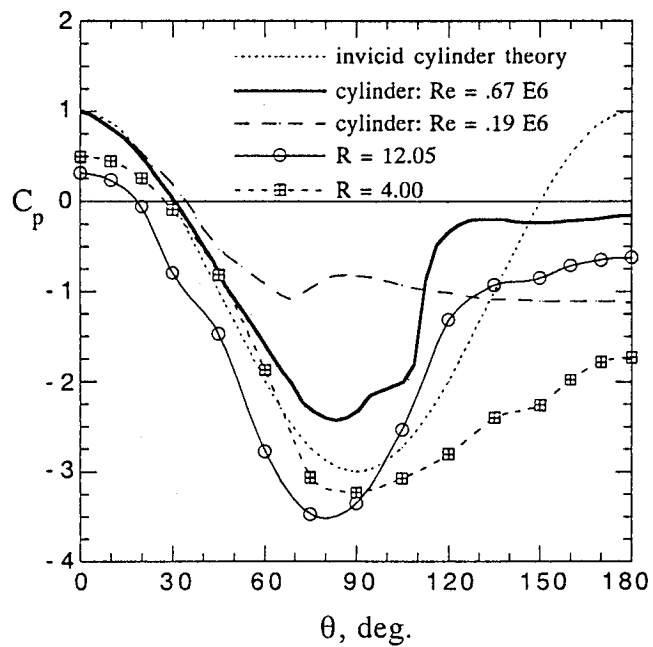


Fig. 15. $C_p$ near jet exit (r/D = 0.58) at $M_j$ = 0.74 for various velocity ratios compared with 2-D cylinder experimental $C_p$[16].

9